The Astrophysical Journal Letters, 903:L1 (6pp), 2020 November 1 https://doi.org/10.3847/2041-8213/abbb9a

A Belt-like Distribution of Gaseous Hydrogen Cyanide on Neptune's Equatorial Stratosphere Detected by ALMA

Takahiro Iino[1], Hideo Sagawa[2], Takashi Tsukagoshi[3], and Satonori Nozawa[4]
[1] Information Technology Center, The University of Tokyo, 2-11-16, Yayoi, Bunkyo, Tokyo 113-8658, Japan; iino@nagoya-u.jp
[2] Faculty of Science, Kyoto Sangyo University, Motoyama, Kamigamo, Kita-ku, Kyoto 603-8555, Japan
[3] National Astronomical Observatory of Japan, 2-21-1 Osawa, Mitaka, Tokyo 181-8588, Japan
[4] Institute for Space-Earth Environmental Research, Nagoya University, Furo-cho, Chikusa-ku, Nagoya, Aichi 464-8601, Japan
Received 2020 August 5; revised 2020 September 25; accepted 2020 September 25; published 2020 October 23

Abstract

We present a spatially resolved map of integrated-intensity and abundance of Neptune's stratospheric hydrogen cyanide (HCN). The analyzed data were obtained from the archived 2016 observation of the Atacama Large Millimeter/submillimeter Array. A $0\farcs42 \times 0\farcs39$ synthesized beam, which is equivalent to a latitudinal resolution of $\sim 20^\circ$ at the disk center, was fine enough to resolve Neptune's $2\farcs24$ diameter disk. After correcting the effect of different optical path lengths, a spatial distribution of HCN emissions is derived over Neptune's disk, and it clearly shows a band-like HCN enhancement at the equator. Radiative transfer analysis indicates that the HCN volume mixing ratio measured at the equator was 1.92 ppb above the 10^{-3} bar pressure level, which is 40% higher than that measured at the southern middle and high latitudes. The spatial distribution of HCN can be interpreted as either the effect of the transportation of N_2 from the troposphere by meridional atmospheric circulation, or an external supply such as cometary collisions (or both of these reasons). From the meridional circulation point of view, the observed HCN enhancement on both the equator and the pole can be explained by the production and accumulation of HCN at the downward branches of the previously suggested two-cell meridional circulation models. However, the HCN-depleted latitude of 60° S does not match with the location of the upward branch of the two-cell circulation models.

Unified Astronomy Thesaurus concepts: Planetary atmospheres (1244); Atmospheric composition (2120); Radio astronomy (1338); Submillimeter astronomy (1647)

1. Introduction

The presence of hydrogen cyanide (HCN) characterizes Neptune's stratospheric composition. The first detection of HCN was made by single-dish millimeter/submillimeter telescopes observing the rotational transitions of $J = 3$–2 and 4–3 (Rosenqvist et al. 1992; Marten et al. 1993). The observed line widths of HCN were significantly narrow as ~20 MHz, indicating that HCN is present in the upper stratosphere. The volume mixing ratio (VMR) determined from $J = 3$–2 and 4–3 observations were 3.0×10^{-10} and 1.0×10^{-9}, respectively. The HCN was restricted to be present at altitudes above the HCN condensation level, 3.5 mbar atmospheric pressure region. Subsequent sensitive disk-averaged observations also identified vertical distributions, and suggested that HCN was present in the region above 0.9–3 mbar, where the condensation cannot occur (Marten et al. 2005; Rezac et al. 2014).

To explain the production of HCN in Neptune's atmosphere, Lellouch (1994) developed a photochemical model of N-bearing species. The production of HCN from dissociated N-atoms was explained by two reactions: $N + CH_3 \rightarrow H_2CN + H$ and $H_2CN + H \rightarrow HCN + H_2$. Two scenarios were proposed for the origin of the N-atoms: (1) infalling of ionized N-atoms transported from Neptune's largest moon, Triton, and (2) the upward transportation of N_2 from the warm troposphere and subsequent dissociation of N_2 by Galactic cosmic rays. The latter scenario suggests the importance of N_2 transportation into the stratosphere by global circulation. The circulation has been inferred by the observations of continuum emissions and tropospheric gases because the atmospheric transportation may cause perturbations in the brightness temperature by adiabatic heating and cooling, and molecular opacity variation (de Pater et al. 2014; Fletcher et al. 2014; Tollefson et al. 2019). Previous studies suggested that the observational signatures of the dry south polar troposphere, cold midlatitudinal stratosphere, and warm equatorial stratosphere are caused by the downward transportation of dry air, adiabatic cooling induced by the upward transportation, and adiabatic heating by the downward transportation, respectively. The suggested upward branch in the meridional circulation could transport N_2 from the troposphere into the stratosphere in the midlatitude, and possibly produce HCN by photochemical reactions in the stratosphere.

In turn, some observations supported an external origin scenario that cometary impact and influx of the interplanetary dust particle supply volatiles to the stratosphere. Such a process is well known for Jupiter, where the collisions of comet Shoemaker–Levy 9 produced a large amount of volatiles such as carbon monoxide (CO), HCN, carbon monosulfide (CS), and H_2O, as long-lived species in the stratosphere (Lellouch et al. 1997; Moreno et al. 2001, 2003; Cavalié et al. 2013; Iino et al. 2016). Among these species, on Neptune, CS and H_2O are particularly important probes of the external volatiles supply because such species cannot pass through the cold tropopause in the gas phase (they are easily condensed in low-temperature environment). Some attempts have been made to detect CS on Neptune (Moreno 1998; Iino et al. 2014), and a recent Atacama Large Millimeter/submillimeter Array (ALMA) observation reported the first detection of CS ($J = 7$–6) on Neptune with a 2.4–21.0×10^{-11} mixing ratio above the 0.5–0.03 mbar pressure level (Moreno et al. 2017). The detection of CS on Neptune reinforces the evidence for a previous cometary

impact that should have supplied HCN, along with CS (and CO) at the same time as occurred on Jupiter.

HCN is also a subject of research for Saturn's largest moon, Titan. HCN has been observed by in situ space- and ground-based observations. Those observations revealed a remarkable seasonal change in Titan's HCN distribution, in which the winter hemisphere has a larger abundance than that of the summer hemisphere (Coustenis et al. 1989, 2007, 2010, 2016; Thelen et al. 2019). In particular, the Cassini spacecraft illustrated HCN enhancement at the winter pole before the summer solstice. HCN abundance measured at 75° S showed ∼1000 times enhancement in two years, from 2012 to 2014 (Coustenis et al. 2016). The inhomogeneous distribution is attributed to effects of global circulation and photochemistry. Vinatier et al. (2015) successfully obtained the seasonal evolution of HCN vertical distribution by analyzing the number of Cassini observation data using the radiative transfer method. They concluded that, in 2011, two years after the vernal equinox, a single north-to-south-pole cell appeared in the meridional circulation, and transported HCN-enriched air to the south pole.

The case of Titan described above is indicative that the spatially resolved observation of volatiles, in particular HCN, could give us a new clue on the atmospheric dynamics and chemistry of Neptune. The ALMA achieves high spatial resolution observation of solar system objects in millimeter and submillimeter wavelengths, whereas previous observations using single-dish telescopes were able to obtain only the disk-averaged spectra of HCN. In this Letter, we first report the spatial distribution of HCN in Neptune's stratosphere obtained with ALMA.

2. Image Synthesis of ALMA Archived Data

We analyzed archived ALMA data of project ID 2015.1.01471.S (PI: R. Moreno) including the HCN ($J = 4$–3) rotational transition at 354.505 GHz, the same project that was used in Moreno et al. (2017). The observations were performed originally to search for isotopologues of major species such as CO and HCN, and minor chemical species such as CS and CH_3CCH on Neptune.

The observation was performed on 2016 April 30 (UTC) using forty-one 12 m antennae. At the observed time, the apparent angular diameter of Neptune was 2.″24. Both the subobserver and subsolar latitude were 26° S. The center frequency of the spectral window used for the analysis was 355.19004 GHz. The total bandwidths of the spectral window and the channel spacing were 1875 and 0.977 MHz (the effective spectral resolution was ∼ 1.13 MHz), respectively. The total observing time of Neptune was 808.1 s.

The Common Astronomy Software Applications package, version 4.6, was used for the reduction of u–v data. We calibrated the raw data using the scripts provided by ALMA. The flux, bandpass, and phase calibrators were the asteroid Pallas and quasars J0006-0623 and J2246-1206, respectively. In the u–v data set, the continuum and line emissions were separated. A CLEAN procedure was used for imaging with the following parameters: 320 × 320 pixels with 0.″025 pixel spacing, "natural" weighting, 0.1 mJy threshold, 0.1 gain, and csclean mode. A circular CLEAN region that had a diameter slightly larger than Neptune was employed with the channel (width = 1) clean mode. The achieved synthesized beam size was 0.″42 × 0.″39, which was fine enough to resolve Neptune's disk spatially.

3. Analysis of Spatial Distribution of HCN Emission

To illustrate the spatial distribution of HCN on Neptune's disk, an integrated-intensity map that integrates the ±30 MHz frequency range, which covers the entire HCN emission line, was produced. The map is shown in Figure 1(a) and exhibits a clear ring-like structure with a ∼0.″95 radius, which has been also reported in an unpublished work using the Submillimeter Array (Moullet & Gurwell 2011). Note that the ring structure is attributed to the increase of the line-of-sight path length in the Neptune atmosphere as the emission angle increases. Figure 1(b) shows the HCN intensity measured at the same emission angle along the 1.″05 and 0.″75 radius circles in Figure 1(a), which can exhibit latitudinal intensity variation without variation of the emission angle. Vertical and horizontal error bars are an rms noise level measured outside the disk and the latitude range included in the synthesized beam, respectively. Eastern and western hemispheric intensities are averaged. For both selected circles, an interesting feature is that the greatest intensity peak is locating at the equator. The lowest intensity values of the both circles locate at 60° S. The peak intensity measured at the equator is 25%–30% higher than the lowest value. In addition, for the 1.″05 circle, a weak intensity peak is also found on the south pole. The intensity difference between 60° S and the south pole is ∼10%.

Figure 1(c) shows the radial HCN intensity profile measured for each pixel and radially averaged profile. A peak located at ∼1″ corresponds to the ring structure shown in Figure 1(a). The radially averaged profile was produced by the polynomial fitting method. The intensity ratio of measured and averaged intensity is shown in Figure 2. While both the vertical and horizontal errors are omitted due to the dense distribution of dots, corresponding errors are the same as in Figure 1(b) and the size of the synthesized beam size, respectively.

To illustrate the latitudinal intensity distribution over the entire disk, an intensity ratio map of measured intensity versus radially averaged intensity was produced (Figure 2(a)). The same method was applied to derive the global continuum emission distribution on Neptune (Iino & Yamada 2018). On the equator, a belt-like HCN-rich region, which corresponds to the latitudinal peaks found in the 1.″05 radius circle in Figure 1(b), is clearly shown. At the southern midlatitude of ∼60° S, a low intensity ratio region is found in the western hemisphere. A latitudinal profile of the intensity ratio is shown in Figure 2(b). For a better visibility of the figure, every third pixel intensity was plotted. The derived structure is similar to that measured along the same emission angle as shown in Figure 1(b). The red curve represents the latitudinally averaged profile of the ratio. The equatorial peak shows a latitudinally symmetrical structure. In addition, a relatively weak peak is found at the south pole. Latitudinal errors corresponding to the synthesized beam size are represented at the bottom of Figure 2(b). At the 60° S region, intensity ratio values can be divided into two groups, which are likely to correspond to a dark spot located in the western hemisphere and other regions on 60° S arc. Considering the self rotation period of Neptune of ∼16 hr, Neptune rotates ∼15° during the observation time. In turn, the difference of intensity between the bright and dark regions on the 60° S arc is ∼10%, which is similar to the systematic error value of ALMA's intensity measurement

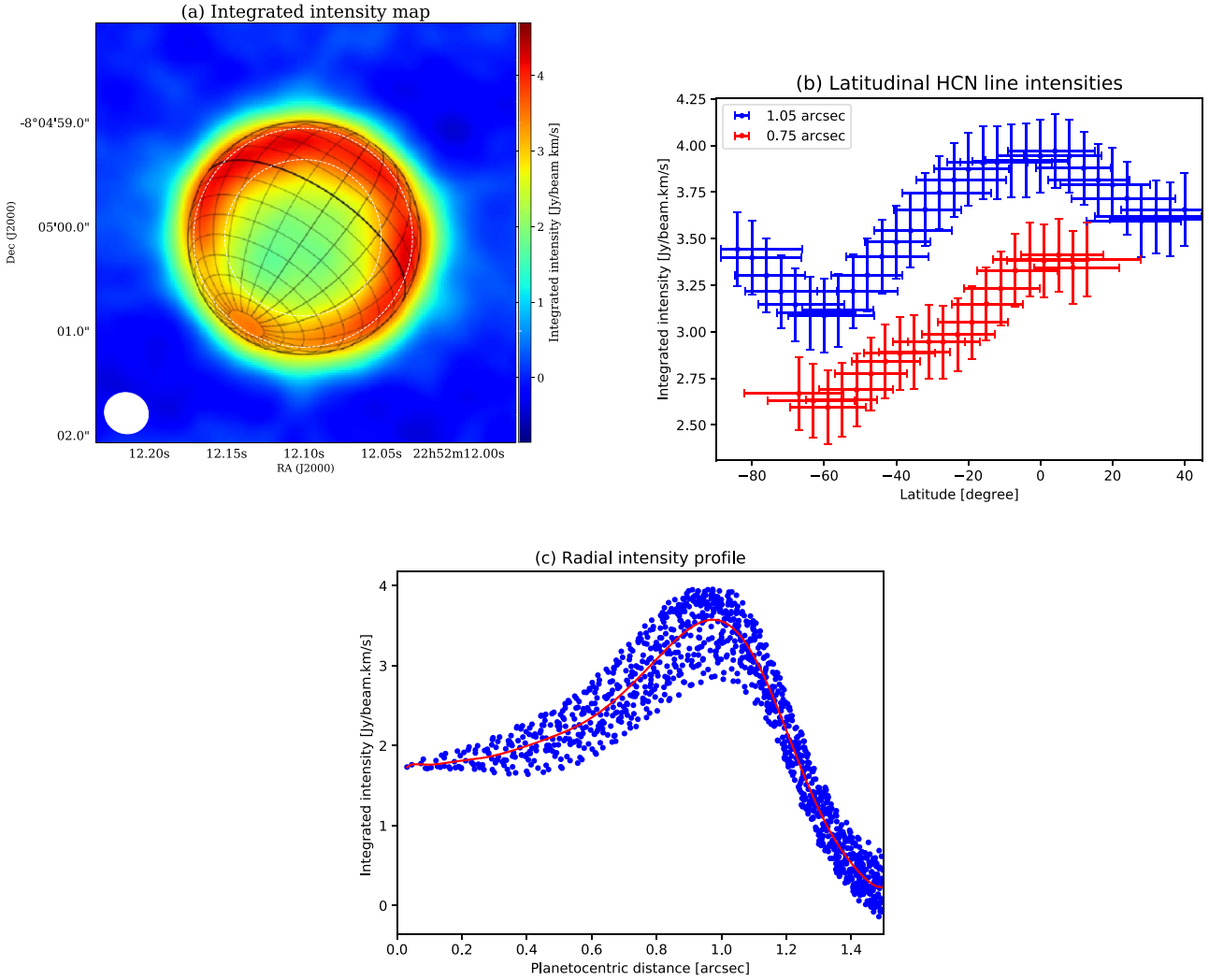

Figure 1. (a) Integrated-intensity map of HCN ($J = 4$–3) for Neptune. The white ellipse at the bottom left illustrates the shape of the synthesized beam. (b) HCN intensity profiles along the 1.″05 and 0 .″75 radius circles indicated by white dashed lines in (a). (c) Radial HCN intensity profile (blue dots) and averaged profile (red curve). Horizontal and vertical error bars are the same as the synthesized beam size, ∼0.″2 and 0.2 Jy beam^{-1} km s^{-1}, respectively.

accuracy. Thus, detection of the HCN depletion spot on 60° S arc is marginal.

4. Radiative Transfer Analysis

The radiative transfer method was employed to estimate the latitudinal difference of HCN abundance between 60° S and the equatorial region by searching the best-fit spectrum. For the calculation, we employed the open-source software Planetary Spectrum Generator (PSG; Villanueva et al. 2018). Because PSG has an online Application Program Interface that is easy to use, one can evaluate our result by reproducing the observed spectra.

Pressure levels of modeled vertical atmospheric structure ranged from 100 to 10^{-4} bar with 40 layers. For the temperature profile, we employed a disk-averaged result retrieved from Fletcher et al. (2010). Gaseous H_2, He, CH_4, CO, and HCN were considered as the atmospheric constituents. Their vertical abundance profiles except for HCN were the initial set of PSG (Marten et al. 2005; Moses 2005; Lellouch et al. 2010). Spectroscopic parameters are as of the HITRAN database. Because PSG can employ a horizontally symmetrical beam, a 0.″41 diameter beam was employed while the true beam shape is slightly elliptical. We attempted to obtain the HCN abundance at two points on 60° S and the equator.

As the vertical HCN profile, a constant molecular VMR above a specific pressure level, p_0, was employed in this study. We have tested some p_0 values in the range from 0.5 to 2.0 mbar pressure level. As a result, we employed a 1.0 mbar pressure level as p_0 because the value could reproduce the observed spectra to a relatively better extent.

The best-fit spectrum for each point was identified within the VMR parameter space by the least-squares method. The $\Delta\chi^2$ technique was used to obtain the error for the fitted parameter (Teanby et al. 2006). The 1σ significance level was used as the error value, corresponding to $\Delta\chi^2$=1.0. The derived VMR and errors for 60° S and the equatorial region were 1.17 ± 0.03 and $1.66^{+0.06}_{-0.03}$ ppb, respectively, above the 1.0 mbar pressure region. Thus, the equatorial region is determined to have 40% higher abundance than that of 60° S region.

Figures 3(a) and (b) show a series of the measured and best-fit spectra. Residuals between the observed and modeled spectra are also shown as red curves with an offset of −5 K. Considering the atmospheric structure, opacity of the HCN line core is derived to be ∼0.3. Because of the thin opacity, the line core is likely to have the sensitivity peak nearly at 1.0 mbar

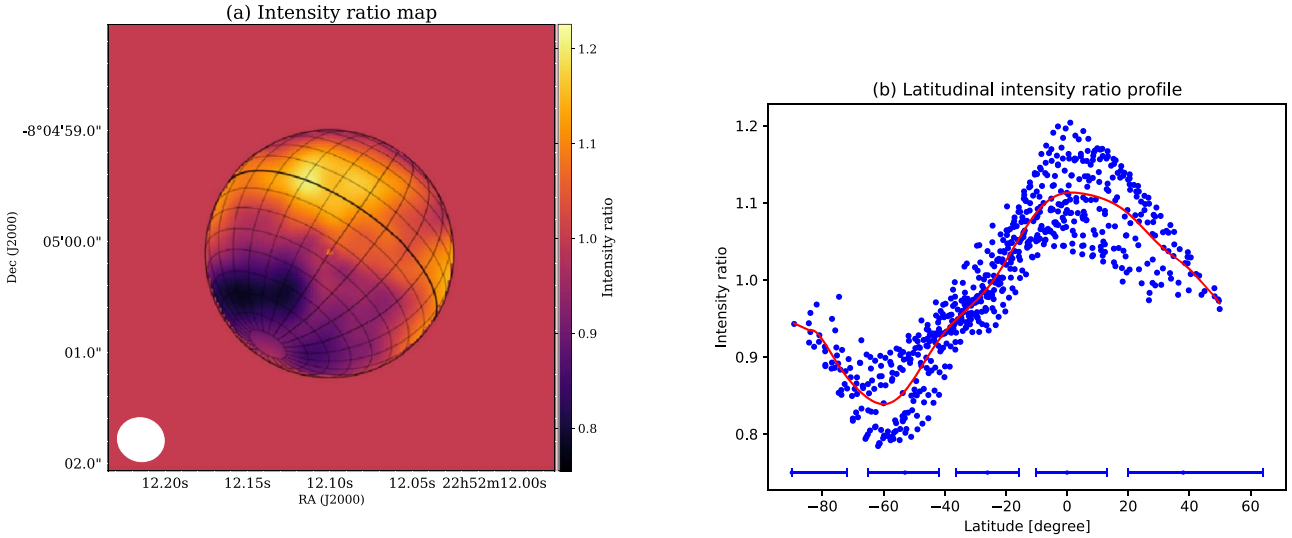

Figure 2. (a) Intensity ratio (measured value vs. radially averaged profile) map of HCN. The white ellipse at the bottom left illustrates the shape of the synthesized beam. (b) Latitudinal profile of the intensity ratio. Blue dots and red curve are for each pixel and the latitudinally averaged profile, respectively. Horizontal error bars at the bottom are latitudinal error measured on the central meridian line.

level. For the equatorial spectra, the ±1.5 MHz frequency region from the line center could not fit well. This result leads to three possible scenarios, that the HCN abundance or temperature decreases, or both decrease in the high-altitude region. However, in this study, we did not attempt to obtain more specific abundance or temperature profiles, because the area of the line center residual is quite small compared with the total area of the emission spectra and the possible effect on the retrieved column density is very limited.

5. Discussion

This new analysis of the spatially resolved ALMA spectroscopic observation data for Neptune indicates that Neptune's stratospheric HCN has a horizontally nonuniform distribution, in which the equator has a ∼30% higher line intensity and ∼40% higher abundance than that of the 60° S region. Possible scenarios that might explain the observed results are discussed from two points of view of the origin of HCN: internal and external sources.

5.1. Possible Sources of HCN Intensity Gradient

Spatial variations in HCN line intensity can be caused both by spatial variations in the temperature of the foreground stratosphere and the background troposphere, and differences in HCN abundance. The variation in stratospheric or tropospheric temperature is equivalent to that of the HCN intensity, because the HCN line core opacity of ∼0.3 is optically thin; thus, its intensity is roughly linear with the temperature variation. To explain the observed maximum 30% intensity variation only by the temperature variation, the spatial temperature difference at the same altitude should have nearly the same ratio as the integrated line intensity variation. Fletcher et al. (2014) retrieved atmospheric temperatures from two observations of Voyager 2 in 1989 and Keck/Long Wavelength Spectrometer in 2003. Above 1.0 mbar, where HCN molecules are present, the inferred temperature variations were no more than 5 K, which are not enough to explain the observed HCN intensity variation. Note that the tropospheric temperature variation measured by 245 and 646 GHz ALMA spatially resolved continuum observations were reported to be smaller than that expected in the stratosphere (Iino & Yamada 2018; Tollefson et al. 2019). Thus, in this study, we consider that the variation in HCN line intensity was caused mainly by a variation in HCN abundance.

5.2. Implication for Global Circulation

The spatial distribution of short-lived trace species is a powerful tool for investigating atmospheric dynamics. The obtained HCN latitudinal gradient shows a morphological similarity with that observed on Titan, where the global single-cell circulation possibly produces a latitudinal abundance difference in which the winter and summer hemispheres exhibit the highest and lowest peaks of HCN, respectively (Coustenis et al. 1989, 2007, 2010, 2016; Thelen et al. 2019). On Titan, similar to the terrestrial Brewer–Dobson circulation, a global single cell in the meridional circulation is likely to transport an N-bearing species depleted air parcel from the summer to winter hemisphere. Various N-bearing species are being produced during the horizontal transportation, and accumulated on the winter pole where the subsiding transportation is present. In addition, the result obtained here is similar to that for Earth's stratospheric ozone (e.g., Wayne 2000), which is also caused by a summer-to-winter single-cell meridional circulation.

On Neptune, various observation techniques have already been used to propose the presence of a global tropospheric and stratospheric circulation. In a reanalysis of Voyager/Infrared Interferometer Spectrometer and Radiometer spectra, Fletcher et al. (2014) concluded there is a global circulation where cold air rises in the midlatitude and subsides both on the equator and the poles. A warm tropospheric equator and pole are likely to be produced by the adiabatic heating induced by the subsiding air. Similarly, de Pater et al. (2014) suggested that upward transportation at midlatitude, ∼40° S, creates a belt-like structure of the tropospheric cloud that is caused by the adiabatic cooling of the rising air parcel. A recent ALMA continuum observation expects that midlatitude upward transportation is present at a relatively lower latitude region, ∼30° S (Tollefson et al. 2019). From a morphological point of

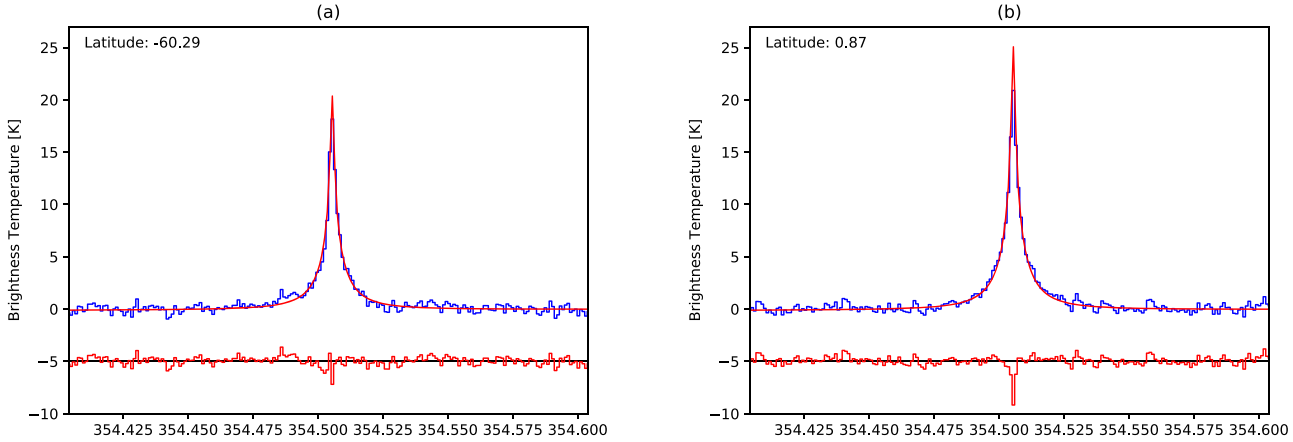

Figure 3. Observed (blue) and modeled (red) HCN spectra measured and derived at 60° S (a) and the equator (b) on the central meridian line. Residual is plotted with a separation of −5 K in the red curve.

view, our obtained HCN distribution map can be connected to the previous observations of the global circulation as follows: the high abundances at the equator and south pole are likely to be due to the accumulation of HCN produced during the horizontal transportation in the same manner as the mechanism of Titan's HCN distribution. Considering the troposphere–stratosphere circulation, N_2 transported to the stratosphere dissociates into N-atom by the photolysis, and leads to HCN production via H_2CN, as mentioned in the 1. HCN enhancements at both the equator and south pole are quite consistent with a two-cell circulation model for the southern hemisphere.

In turn, the HCN-depleted region observed at 60° S disagrees with the location of the upward branch of the two-cell circulation model (the circulation model shows the upward transportation at 40° S). Although the reason for this remains for further study, it should be noted that our study probes the upper stratosphere while the previously suggested two-cell meridional circulation model has been mainly based on observations of the upper troposphere. An effective use of HCN maps may bring an additional constraint to the atmospheric circulation at higher altitudes. In addition, because of the coarse resolution of this analysis, 40° S and 60° S regions were not resolved clearly. Thus, a new observation with a higher spatial resolution enables us to determine the latitude of the HCN-depleted belt.

5.3. External Source Model

A large cometary impact is also a possible cause of the observed HCN distribution. Strong evidence for such an impact was previously provided by the presence of CS (Moreno et al. 2017) and by the CO-rich upper stratosphere (Lellouch et al. 2005; Hesman et al. 2007; Fletcher et al. 2010). Because no S-bearing species can be supplied from the troposphere, CS is considered to have only a cometary origin. Thus, it is also possible for HCN to be supplied by a past cometary impact, likely an impact at the equator. To evaluate the cometary impact hypothesis, a new analysis of the latitudinal distribution of CS is crucial. If CS shows the equatorial enhancement seen in HCN, the impact hypothesis is strongly supported. It is noted that our observation shows HCN enhancement at the south pole as well. Such a latitudinal distribution does not fit well with a simple meridional diffusion of HCN from a single collision.

5.4. Future Perspectives

This study presented that a spatially resolved HCN observation has significant potential for providing various information for discerning the atmospheric circulation and/or a past cometary impact. As mentioned in Section 5.3, highly sensitive observation of CS to illustrate its spatial distribution, along with the determination of the 3D distribution of CO, would strongly constrain the cometary impact scenario. Also the spatial distribution of H_2O, which is not observable by ALMA, is crucial to evaluate the scenario as for the case for Jupiter (Cavalié et al. 2013). In addition, precise observations to determine the $^{14}N/^{15}N$ isotopic ratio in HCN may constrain its source and production process. For example, on Jupiter, a large nitrogen isotopic fractionation in HCN (4.3–16.7 times higher than the typical solar system value) was detected (Matthews et al. 2002). This fractionation may be caused by the thermo-chemical processed induced by the cometary collision. In addition, on Titan, a different isotopic fractionation between N_2 and its daughter species, HCN, is known (Hidayat et al. 1997; Gurwell 2004; Molter et al. 2016). A theoretical chemical model suggests that the nitrogen-bearing species is fractionated in a different extent according to different dissociation processes of N_2 (Dobrijevic & Loison 2018). These applications to other planets and satellites lead one to expect that a new determination of the nitrogen isotopic ratio in Neptune HCN will provide new implication on its origin.

This Letter makes use of the following ALMA data: ADS/JAO.ALMA#2015.1.01471.S. T.I. wishes to thank Satoru Nakamoto and Yuma Nakayama of Nagoya University for their dedicated contribution on the preliminary analysis of the ALMA data.

This work was financially supported by a Telecommunications Advancement Foundation, JSPS Kakenhi (17K14420 and 19K14782) and an Astrobiology Center Program of National Institutes of Natural Sciences grants. ALMA is a partnership of ESO (representing its member states), NSF (USA) and NINS (Japan), together with NRC (Canada), MOST and ASIAA (Taiwan), and KASI (Republic of Korea), in cooperation with the Republic of Chile. The Joint ALMA Observatory is operated by ESO, AUI/NRAO and NAOJ.

Software: Astropy (Robitaille et al. 2013), PSG (Villanueva et al. 2018).

ORCID iDs

Takahiro Iino https://orcid.org/0000-0003-1502-178X
Hideo Sagawa https://orcid.org/0000-0003-2064-2863
Takashi Tsukagoshi https://orcid.org/0000-0002-6034-2892
Satonori Nozawa https://orcid.org/0000-0002-4359-6524

References

Cavalié, T., Feuchtgruber, H., Lellouch, E., et al. 2013, A&A, 553, A21
Coustenis, A., Achterberg, R. K., Conrath, B. J., et al. 2007, Icar, 189, 35
Coustenis, A., Bézard, B., & Gautier, D. 1989, Icar, 82, 67
Coustenis, A., Jennings, D. E., Achterberg, R. K., et al. 2016, Icar, 270, 409
Coustenis, A., Jennings, D. E., Nixon, C. A., et al. 2010, Icar, 207, 461
de Pater, I., Fletcher, L. N., Luszcz-Cook, S., et al. 2014, Icar, 237, 211
Dobrijevic, M., & Loison, J. C. 2018, Icar, 307, 371
Fletcher, L. N., de Pater, I., Orton, G. S., et al. 2014, Icar, 231, 146
Fletcher, L. N., Drossart, P., Burgdorf, M., Orton, G. S., & Encrenaz, T. 2010, A&A, 514, A17
Gurwell, M. A. 2004, ApJ, 616, L7
Hesman, B. E., Davis, G. R., Matthews, H. E., & Orton, G. S. 2007, Icar, 186, 342
Hidayat, T., Marten, A., Bézard, B., & Gautier, D. 1997, Icar, 182, 170
Iino, T., Mizuno, A., Nakajima, T., et al. 2014, P&SS, 104, 211
Iino, T., Ohyama, H., Hirahara, Y., Takahashi, T., & Tsukagoshi, T. 2016, AJ, 152, 179
Iino, T., & Yamada, T. 2018, AJ, 155, 92
Lellouch, E. 1994, Icar, 108, 112
Lellouch, E., Bézard, B., Moreno, R., et al. 1997, P&SS, 45, 1203
Lellouch, E., Hartogh, P., Feuchtgruber, H., et al. 2010, A&A, 518, L152
Lellouch, E., Moreno, R., & Paubert, G. 2005, A&A, 40, L37
Marten, A., Gautier, D., Owen, T., et al. 1993, ApJ, 406, 285
Marten, A., Matthews, H., Owen, T., et al. 2005, A&A, 429, 1097
Matthews, H. E., Marten, A., Moreno, R., & Owen, T. 2002, ApJ, 580, 598
Molter, E. M., Nixon, C. A., Cordiner, M. A., et al. 2016, AJ, 152, 42
Moreno, R. 1998, PhD Thesis, Université Paris VI
Moreno, R., Lellouch, E., Cavalié, T., & Moullet, A. 2017, A&A, 608, L5
Moreno, R., Marten, A., Biraud, Y., et al. 2001, P&SS, 49, 473
Moreno, R., Marten, A., Matthews, H. E., & Biraud, Y. 2003, P&SS, 51, 591
Moses, J. I. 2005, JGRE, 110, E08001
Moullet, A., & Gurwell, M. 2011, in EPSC-DPS Joint Meeting (Göttingen: Copernicus), 1153
Rezac, L., de Val-Borro, M., Hartogh, P., et al. 2014, A&A, 563, A4
Robitaille, T. P., Tollerud, E. J., Greenfield, P., et al. 2013, A&A, 558, A33
Rosenqvist, J., Lellouch, E., Romani, P., Paubert, G., & Encrenaz, T. 1992, ApJL, 392, L99
Teanby, N., Fletcher, L. N., Irwin, P. G. J., Fouchet, T., & Orton, G. S. 2006, Icar, 185, 466
Thelen, A. E., Nixon, C., Chanover, N., et al. 2019, Icar, 319, 417
Tollefson, J., de Pater, I., Luszcz-Cook, S., & DeBoer, D. 2019, AJ, 157, 251
Villanueva, G. L., Smith, M. D., Protopapa, S., Faggi, S., & Mandell, A. M. 2018, JQSRT, 217, 86
Vinatier, S., Bézard, B., Lebonnois, S., et al. 2015, Icar, 250, 95
Wayne, R. 2000, Chemistry of Atmospheres (Oxford: Oxford Univ. Press)